

## 10

# Stretchable Electronic and Optoelectronic Devices Using Single-Crystal Inorganic Semiconductor Materials

*Dae-Hyeong Kim, Nanshu Lu, and John A. Rogers*

### 10.1

#### Introduction

##### 10.1.1

#### Materials Selection for High-Performance Stretchable Electronics

High-quality monocrystalline inorganics, such as silicon and group III–V semiconductors, have served as the dominant active materials in electronics since the field effect transistor (FET) was invented 60 years ago [1, 2]. By far, the most widely used semiconductor for microprocessors and memory devices is silicon, due to a remarkable convergence of properties, processability, and earth abundance [3, 4]. Optoelectronics, however, requires direct bandgap materials [5]. Here, III–V semiconductors, such as gallium arsenide (GaAs) and gallium nitride (GaN) [6], are important. These same materials can also be useful in high power and radio frequency electronics [4, 7]. In parallel development efforts of recent years, organic semiconductors, ranging from the small molecules such as pentacene to polymers such as poly(phenylenevinylene) [8–11], have been explored as alternatives to these inorganics, where the focus is on flexible devices for display, lighting, photovoltaics, and related applications [12–18]. In such uses, organics offer advantages compared with inorganics (implemented in the conventional way), such as ability to process over large areas, at low temperatures, and on mechanically bendable plastic substrates, in some cases by solution printing and other nonvacuum procedures [10, 12, 13, 19]. A challenge is that although the quality and performance of such organic semiconductors are improving steadily over time, to a point that they are now suitable for several important applications (e.g., paper-like display devices) [17, 20], many key attributes remain inferior to inorganic counterparts. These deficiencies limit the performance and functionality, particularly in integrated circuits [4, 21, 22]. Current research seeks to address these issues with semiconductor nanomaterials, ranging from carbon nanotubes and graphene to inorganic nanowires/ribbons/membranes, designed for similar applications and, ultimately, for new classes of devices that offer reversible mechanical responses to large strain deformations [3, 23–30].

The types of stretchable electronic systems that form the focus of this chapter integrate such materials into device components joined by specialized mechanical bridges and electrical interconnects, on elastomeric substrates to achieve systems that offer not only the ability to bend, like widely explored flexible electronic devices, but also to stretch, twist, fold, wrap curvilinear surfaces and otherwise deform in ways that involve large ( $>1\%$ ) strains [31–34]. These properties expand engineering design options far beyond those possible with conventional high-performance technologies, all of which rely on planar, rigid semiconductor wafers as substrates, but in ways that involve minimal sacrifices in electrical functionality. Uses in components that intimately integrate with the human body (i.e., bio-integrated electronics) [35–40] and those that derive design inspiration from biology (i.e., bio-inspired devices) [41–44] are particularly interesting, and would be impossible to achieve in any other way. A key challenge in engineering is to manage stresses and strains in the resulting hybrid hard/soft material constructs [45, 46]. In particular, although the substrates have low modulus (0.1–10 MPa), and are highly elastic and stretchable, thereby providing necessary restoring forces to induced deformations, the inorganic active materials, and even certain of the insulators and metals, have, by comparison, high modulus (100–200 GPa) and are brittle, with fracture strains of  $\sim 1\%$  [9–11]. As a result, strategic geometric designs in materials and circuit layouts, guided by quantitative mechanics modeling, are central to research and development in this field [28, 30, 47–55]. A useful baseline of strategies and capabilities in important application areas now exist, as described in the next section.

### 10.1.2

#### **Monocrystalline Inorganic Semiconductors in Stretchable Designs**

Various schemes have been developed to accommodate large, system-level deformations without significantly straining the electronics or active materials, as summarized in Figure 10.1. The maximum bending-induced strain and the bending stiffness of a beam are proportional to the beam thickness and the cube of this thickness, respectively [56]. As a result, reducing the thickness of the active materials is the most straightforward way to enhance their flexibility. Ultrathin material structures, such as wires, tubes, ribbons, or membranes, are useful, in this sense. Although many methods for growing nanomaterials of this type now exist [57, 58], a practical route that builds on established electronic materials technology involves lithographically patterned etching of semiconductor wafers, in many cases pre-processed to form, as examples, selectively doped regions and/or integrated passivation layers or dielectrics (e.g., thermal oxide) [28, 30, 59–63]. In most cases, wet etching eliminates an underlying sacrificial layer, or anisotropically removes layers of a bulk material, to release large quantities of well-defined nanomaterial structures. Techniques of transfer printing can then be used to integrate and bond these materials onto elastomeric substrates, often configured in a state of tensile strain (i.e., prestrain) [64]. Releasing this prestrain induces compression and hence controlled buckling of the bonded nanomaterials [28, 47]. The overall hybrid

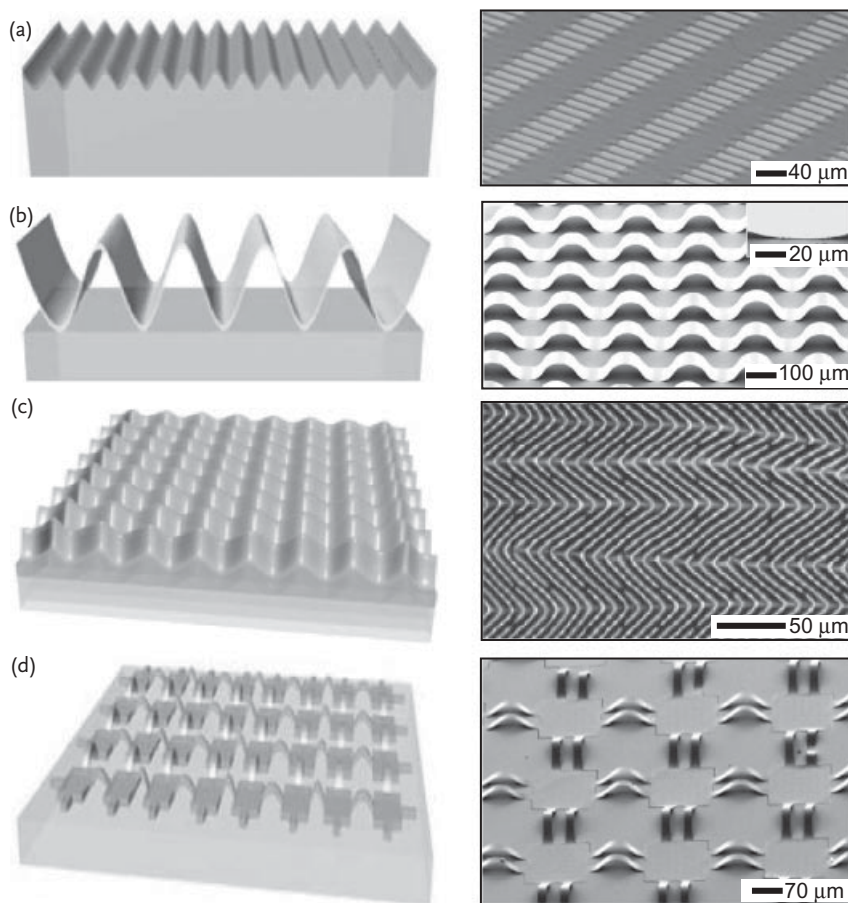


**Figure 10.1** Four different design strategies for stretchable single crystalline inorganic materials on elastomeric supports: schematic illustrations (left) and corresponding

micrographs (right) of one-dimensional (a) “wavy” and (b) “noncoplanar” cases and two-dimensional (c) “wavy” and (d) “noncoplanar” examples.

structure that results from this process can accommodate repeated large strains through changes in the geometries of the patterns of buckling, much like an “accordion bellows.” Stretching can occur up to the point where the buckling structures disappear, typically at a level comparable to the prestrain itself.

Different control parameters can be used to tune the buckling geometry, in ways that optimize the range of stretchability, guided by mechanics modeling. For example, depending on the direction of prestrain (uniaxial or biaxial), the buckling patterns can be either one-directional sinusoidal (Figure 10.1a and b) or two-dimensional herringbone (Figure 10.1c) [28, 30, 41, 47]. The wavelengths and amplitudes of these structures are determined by the prestrain, the thickness of the

membranes/ribbons, and the elastic mismatch between these materials and the substrates. Increasing the prestrain leads to higher amplitudes and larger stretchability, up to some point when the buckling-induced strains in the membranes/ribbons approach their fracture thresholds. More advanced schemes involve open mesh structures, with control of the areas of bonding to the elastomer substrates. In such cases (Figure 10.1b and d) noncoplanar structures form as a result of releasing the prestrain, due to local delamination in the unbonded regions. Detailed fabrication procedures and mechanics analysis can be found in references [41].

### 10.1.3

#### **Bio-integrated Electronics**

One of the most promising applications of stretchable electronics is in health monitoring devices and advanced surgical tools that involve intimate, soft integration with the human body [35–40]. Conventional wafer-based electronics are intrinsically incompatible with soft, curvilinear, and dynamic surfaces of biological tissues [35, 36]. Stretchable systems, by contrast, can be designed with levels of softness and deformability that match, almost perfectly, the mechanics of major organs such as the skin, heart, and brain. The potential applications include neural and cardiac surgical devices, skin-like “epidermal” electronic monitors, intelligent prosthesis, and so on [35–38]. Such devices must also be biocompatible on timescales relevant to their respective modes of use; they require, in certain cases, the capacity to operate during complete immersion in bio-fluids, and they cannot cause unwanted rises in temperature or other effects that lead to tissue degradation. Furthermore, large-area coverage, with distributed, high-speed multiplexing and amplification, is often important with temporal and spatial resolution, compatible with the physiology. For most clinically relevant uses, submillimeter spatial and submillisecond temporal resolution are required [36]. These requirements impose significant challenges on the technology, most of which can be met using approaches that build on the ideas of Figure 10.1, in circuits described in the following.

## **10.2**

### **Stretchable Circuits**

#### 10.2.1

##### **Wavy Electronic Devices and Circuits**

Stretchable electronic devices can be fabricated using shape engineered inorganic materials, in layouts similar to those shown in Figure 10.1. As a simple example, stretchable pn junction diodes can be formed using wavy, predoped silicon nanoribbons by depositing Al through a shadow mask to form electrodes [28]. This same concept can apply directly, to chip-scale flexible integrated circuits, with ultrathin layouts and neutral mechanical plane (NMP) designs. In this case, a 2D wavy

structure, as a generalized version of the herringbone layouts of Figure 10.1, is created at the last step of fabrication. The full fabrication flow involves, as a first step, the transfer printing of doped nanoribbons/membranes onto an ultrathin polyimide substrate supported by a rigid handle wafer. The other layers needed to form transistors, diodes, resistors, and other components in integrated circuits are then formed using conventional semiconductor device fabrication processes. The completed circuit is lifted from the handle wafer and transfer printed onto a prestrained elastomeric substrate, bonded across the entire interface. Releasing the prestrain leads to wavy circuit layouts. To minimize bending-induced strain, all the devices involve passivation layers designed such that semiconductors and metals lie near the NMP [31, 32, 41]. Device examples appear in Figure 10.2 [31].

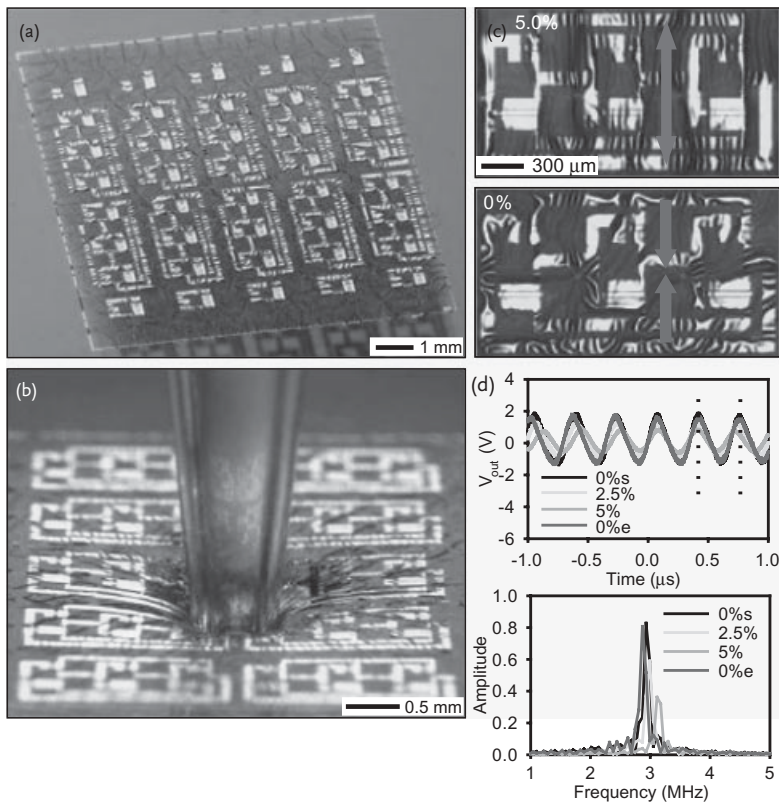


**Figure 10.2** (a) Image of an array of silicon CMOS integrated circuits (10 three-stage ring oscillators, five inverters, and five isolated p and n channel transistors) in a wavy configuration on a PDMS substrate. (b) Image of a stretchable circuit mechanically deformed by applying a downward force near

the center with a glass rod. (c) Optical images at zero and  $\sim 5\%$  tensile strain applied in the vertical direction. (d) Electrical characterization of a three-stage ring oscillator at different applied strain (0%, 2.5%, and 5%, left frame), evaluated in the time and frequency domains.

Figure 10.2a shows p and n type transistors (top), complementary MOS (CMOS) circuits (bottom), and CMOS three-stage ring oscillators (center), in wavy layouts. The illumination conditions highlight the valleys in the wavy structures as dark regions. Circuits configured in this manner can tolerate significant deformation, as shown in Figure 10.2b, where a plastic rod presses into the center of circuit consisting of an array of wavy ring oscillators.

Figure 10.2c and d shows magnified images of a deformed wavy circuit and its detailed characterization results [31]. Three wavy CMOS inverters connect to form three-stage ring oscillators. While regular, repetitive sinusoidal/herringbone structures are generated in simple nanoribbons/membranes (see Figure 10.1a and c), more complicated and random buckles form in the case of Figure 10.2 due to complex spatial configurations of devices and interconnections as well as differences in mechanical properties of the circuit components. Upon application of external force, the spatial layouts, wavelengths, and amplitudes of buckles of the ring oscillator change to accommodate the resulting deformations, while avoiding material strains that would otherwise lead to mechanical fracture (Figure 10.2c). The circuit shows an oscillation frequency around  $\sim 3$  MHz with a 5 V supply voltage and minimum variation under external strains up to  $\sim 5\%$  (Figure 10.2d). This circuit-level buckling strategy can be applied to even more complicated and generalized integrated circuits, such as differential amplifiers [31] and others.

### 10.2.2

#### Noncoplanar Electronic Devices and Circuits

Even though the wavy circuit in Figure 10.2 provides stable electrical operation under reversible stretching without mechanical damage, its maximum stretchability is limited to below  $\sim 10\%$ . Circuits for use in textiles, bio-integrated monitors, and other systems often, however, require stretchability of tens to hundreds of percent [37]. To satisfy such demands, noncoplanar strategies of Figure 10.1b and d can be adopted (Figure 10.3a) [32]. The most effective layout involves active electronic components patterned into an array of isolated islands, with thin, narrow interconnects. Selective bonding of the islands to the substrate causes these interconnect bridges to delaminate and buckle out of the plane of the circuit, upon release of the prestrain. In this configuration, most of the deformations associated with applied strains occur in these noncoplanar, arc-shaped interconnects. A scanning electron microscope (SEM) image of inverters that use this type of design, in a deformed state is shown in Figure 10.3b. Such structures are capable of complex, multidirectional deformations (Figure 10.3b and c).

Finite element modeling (FEM) can quantitatively determine the distributions of strain, as shown in Figure 10.3d. According to these results, strains maximize at the crests of the bridges, but their magnitudes remain well below the yield strains of the metal thin films, which are located at the NMP. The strains in the islands are almost negligible. The effectiveness of such designs and strain management strategies are confirmed by stretching tests on a ring oscillator (Figure

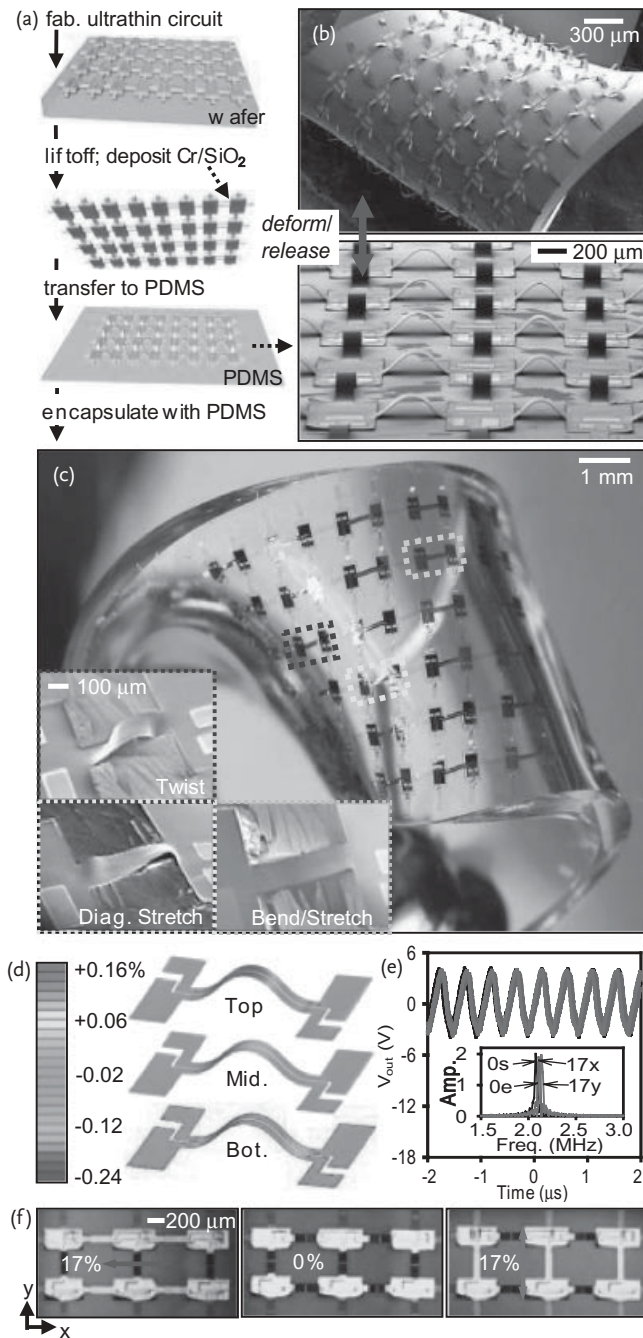


**Figure 10.3** (a) Schematic diagrams of the process for fabricating noncoplanar stretchable CMOS inverters on PDMS. (b) SEM image of an inverter array in flat (bottom) and deformed (top) configurations. (c) Image of a deformed stretchable CMOS inverter array. The inset shows magnified SEM images of a CMOS inverter under different modes of deformation: twisting

(top), diagonal stretching (bottom), and normal stretching (right). (d) Strain distribution evaluated by FEM at the top (PI), middle (metal), and bottom (PI) layers of an inverter. (e) Electrical characterization of a three-stage ring oscillator at different applied strains (0% start, 0% end, 17%  $x$  and  $y$  directions) and (f) corresponding images.

10.3e), where microscope images of undeformed and stretched (by 17% in  $x$  and  $y$  directions) states appear in Figure 10.3f.

### 10.2.3

#### **Electronic Circuits with Serpentine Interconnects**

A further optimization of the structures of Figure 10.3 involves replacement of the straight bridges with narrow, serpentine shapes, to further increase the stretchability and to eliminate the requirement for use of prestrain. To keep the strain below the metal yield point ( $\sim 1\%$ ), while still maintaining high stretchability, changing interconnects from straight to serpentine becomes a natural solution because the rotation of the meandering interconnects can accommodate applied deformation without straining the material [32]. A key aspect in design is that such interconnects, when constrained by bonding to the underlying substrate, have limited freedom of movement. Even for thin and long serpentes in Figure 10.4a, a tensile strain of 60% induces severe cracks that can quickly lead to circuit failure under repetitive loading. Releasing the serpentine interconnects from the substrate, using the selective bonding and noncoplanar concepts of Figure 10.3, allows free rotation and twisting, thereby to enable much improved compliance and stretchability. To compare the mechanics of coplanar and noncoplanar structures, serpentes of the same shape, as shown in Figure 10.4a, were fabricated (Figure 10.4b and c) [65]. Upon stretching to 60%, FEM shows that the maximum principal strains in coplanar and noncoplanar structures are 6.8% and 0.177%, respectively.

### 10.2.4

#### **Stretchable Electronic Devices on Unconventional Substrates**

An additional advantage of stretchability in circuits is that it allows their integration with nearly any type of support. Unconventional substrates of interest include fabrics, leathers, vinyl, and papers for applications on gloves, curtains, shirts, and bags [33, 63, 66, 67]. Stretchable devices can be mounted on such surfaces using the techniques of transfer printing. Here, ultrathin circuits with stretchable layouts are first fabricated on a carrier wafer by following the procedures explained in the previous sections. The resulting circuit can then be retrieved with a PDMS stamp and printed onto various substrates coated with a thin layer of PDMS [64].

The thin PDMS serves three major purposes. First, it provides adhesion between the substrates and ultrathin circuits. In this case, the covalent bonds that spontaneously form between  $\text{SiO}_2$  deposited on the back side of the circuit and activated surface of the PDMS yield a strong mechanical coupling, which can also be spatially patterned for noncoplanar designs mentioned previously [64]. Second, the PDMS can planarize the surfaces of rough substrates to further facilitate this bonding process. The third role of the PDMS is that it serves as a strain isolation interlayer between the bottom substrate and the top devices [66, 68]. The consequence is that a simple, thin coating of PDMS can act as an adhesion layer,

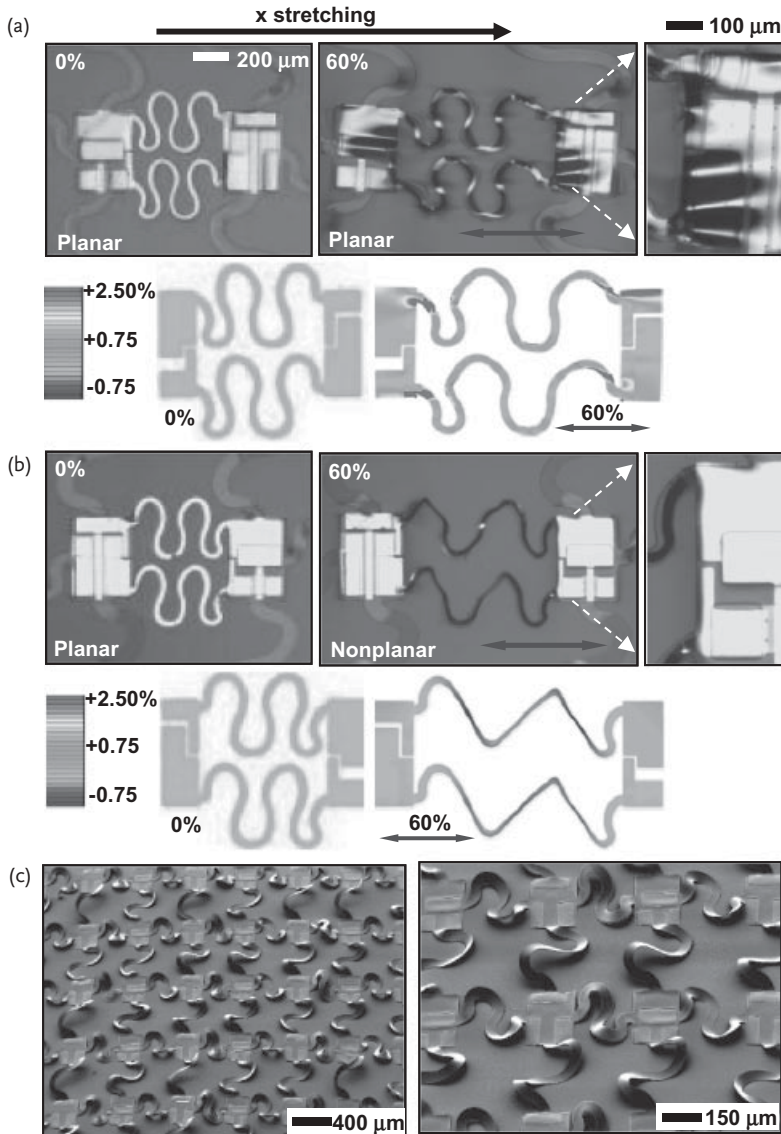


**Figure 10.4** Optical microscope images (top) and maximum principal strain distributions (FEM simulation, bottom) for a CMOS inverter with serpentine interconnects in (a) coplanar and (b) noncoplanar layout before and after deformation. Magnified

images (right top) show the differences in wrinkling and induced strain between these two cases. (c) SEM images of a CMOS inverter array with noncoplanar interconnects.

a planarizing film, and a means to accomplish strain isolation, all in way that only minimally alters the mechanical properties (e.g., bending stiffness) of the substrate.

As examples, arrays of silicon CMOS inverters have been successfully built on gloves and sheets of paper, the latter as demonstrated on the most challenging region, that is, the finger joint, where the largest deformation occurs. Two types of gloves, vinyl and leather, were used, as shown in Figure 10.5a and b, respec-

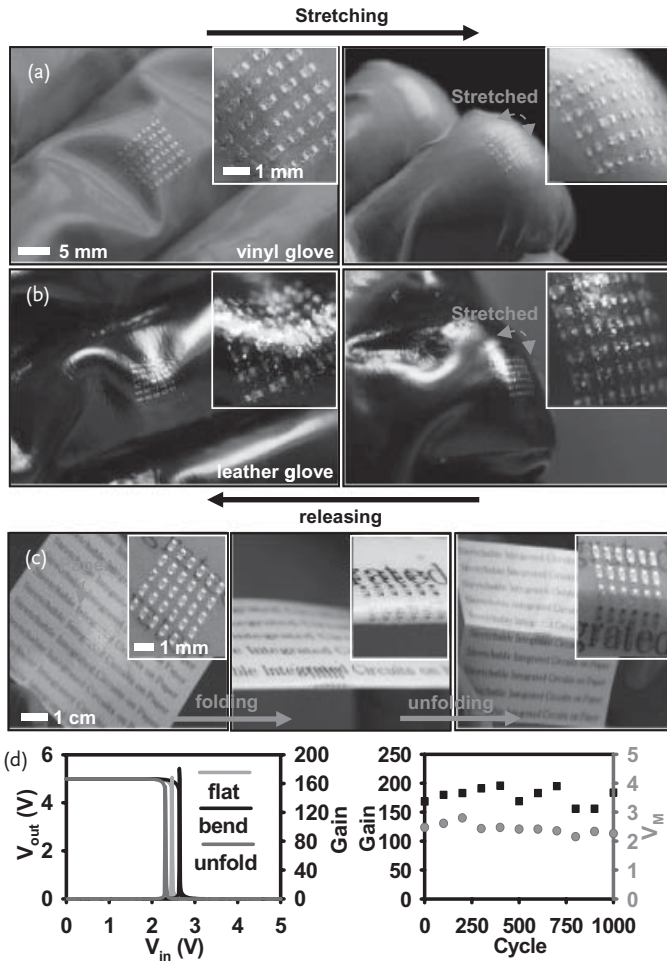


**Figure 10.5** Optical images of an array of stretchable CMOS inverters at the finger joint of (a) vinyl and (b) leather gloves. Moving the fingers stretches and releases the devices. The inset shows a magnified view. (c) Images of an array of inverters on a paper substrate, in a flat (left), folded (center), and

unfolded (right) state. The inset shows a magnified view. (d) Electrical characterization of an inverter on a paper substrate at three different states (flat, folded, and unfolded, left frame). The right frame shows the result of 1000 cycles of folding and unfolding.

tively. For both cases, thin PDMS coatings prepared the surfaces for transfer of ultrathin inverters. When the fingers bend and unbend, the inverters are stretched or released. The compliant serpentine bridges accommodate external strains without any mechanical constraint to the finger motion. Stretching cycles of more than 1000 times, induced by finger motion, cause little or no variations in the electrical properties [66]. Such circuits can also be integrated on paper. Paper, as a portable, light-weight, biocompatible, and low-cost substrate, is not very stretchable, but it can be folded to small radii of curvature to thereby induce significant strains on the surfaces. A series of bending, folding, and unfolding tests on CMOS circuits printed onto paper was carried out and electrical performance was characterized, as shown in Figure 10.5c and d. Cycling tests following this sequence up to 1000 times verifies the stability of operation under these conditions (inverter threshold voltage change  $\leq \pm 0.4$  V, gain change  $\leq \pm 10\%$ ) [66].

### 10.3

#### Application of Stretchable Designs to Microscale Inorganic Light Emitting Diodes ( $\mu$ -ILEDs)

##### 10.3.1

##### Stretchable $\mu$ -ILED Arrays

Conventional flat panel displays, emissive indicators, and solid state lighting systems have limitations in many applications due to the rigidity of the substrates that are commonly used. Advantages in flexibility and lightweight construction make the concepts of stretchable electronics, as described in the previous section, ideal for next-generation lighting and display systems, when implemented with emerging classes of microscale inorganic LEDs (i.e.,  $\mu$ -ILEDs) [69]. A notable aspect of the design is that the strategies for stretchable electronics can be used, with little change, for application in  $\mu$ -ILEDs because the mechanics does not critically depend on the detailed moduli (or materials composition) of the devices [33, 70]. As with electronics, stretchable  $\mu$ -ILEDs can be integrated onto nearly any surface, from paper-like portable personal electronics to large-area commercial displays, both of which are expected to have huge market potential. By comparison with organic light emitting diodes, the obvious alternative, inorganic devices offer improved stability, brightness, and efficiency. A set of examples of stretchable  $\mu$ -ILEDs appear in Figure 10.6 [70]. To make these particular devices, single crystalline AlInGaP, designed for red light emission, is epitaxially grown in suitable multilayer stacks on GaAs wafers. Pixels of  $\mu$ -ILED are defined by processing the material while on the wafers using photolithography and other conventional procedures. The devices are then transfer printed onto polymeric substrates after releasing them from the underlying wafer by undercutting sacrificial layers of AlAs, epitaxially formed beneath the active layers of the devices. Photodefined polymeric “anchors” are placed at the corners of each undercut  $\mu$ -ILED to prevent them from being washed into the etchant. Transfer printing selected sets of these

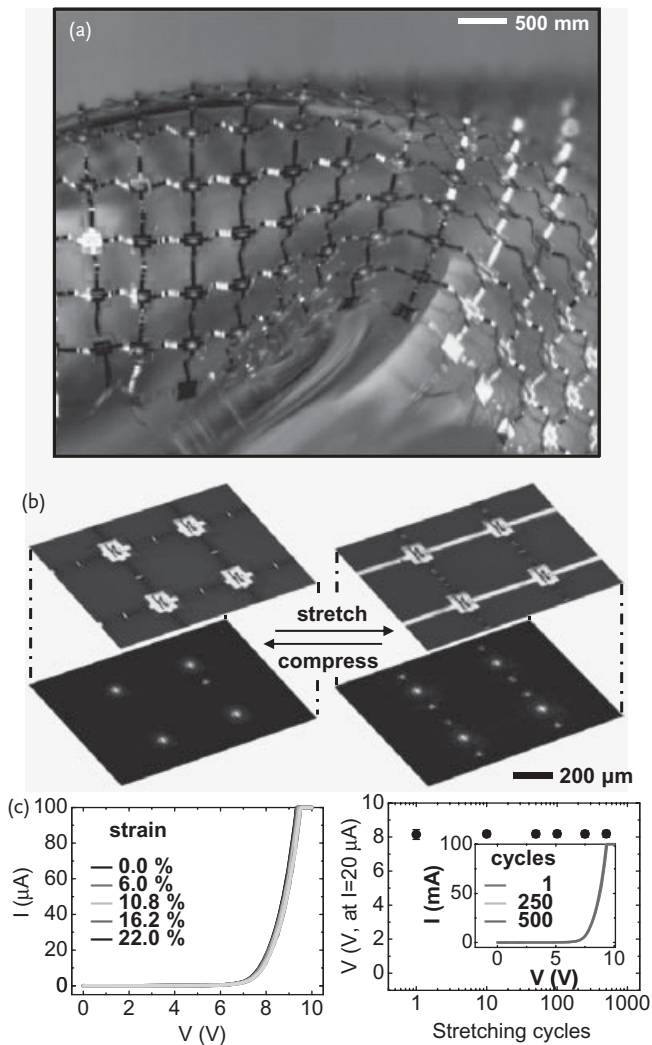


**Figure 10.6** (a) Image of a deformed stretchable  $\mu$ -ILED array. (b) Two-dimensional stretching images of four  $\mu$ -ILEDs. (c) Current–voltage curves at different applied strain (left) and results for repetitive stretching tests, to 1000 cycles (right).

devices, in a step-and-repeat mode, to a carrier glass substrate coated with thin layers of polymers (epoxy/polyimide [PI]/poly(methylmethacrylate) [PMMA]), etching openings for the electrical contacts and then forming interconnects completes the formation of arrays of  $\mu$ -ILEDs. A subsequent layer of polymer spin-casted on top locates the active materials near the NMP. A final reactive ion etching step removes polymer from regions between the pixels and defines the geometries of the joining interconnects. A second transfer printing process moves the inter-

connected, mesh configurations of  $\mu$ -ILEDs onto elastomeric substrates to finish the fabrication. A representative device is shown in Figure 10.6a. Noncoplanar structures consisting of straight-bridge interconnects joining rectangular device islands to provide wide-ranging stretchability and multidirectional deformability (Figure 10.6a). Even after a thousand cycles of stretching, negligible changes in electrical performance are observed (Figure 10.6b and c).

The same strategies for increasing the stretchability in CMOS circuits can be applied to  $\mu$ -ILEDs. In particular, ultrathin noncoplanar serpentine interconnects (Figure 10.7a) enable reliable operation during both in-plane (Figure 10.7) and out-of-plane (Figure 10.8) deformations [33]. Figure 10.7b–d show SEM images of one-dimensional, in-plane stretching of one pair of  $\mu$ -ILEDs, strain distributions determined by FEM and images of a  $6 \times 6$   $\mu$ -ILED array, respectively. The interconnects accommodate applied strain by free rotation and twisting (Figure 10.7b). FEM simulation indicates that the peak strain observed in the metal interconnect layer is less than 0.2%, which is much below the yield strain (Figure 10.7c). The strains in  $\mu$ -ILED islands are  $\sim 100$  times smaller than those of the interconnects [33]. The emission evaluated at various points during thousands of cycles of stretching in both horizontal and diagonal directions remains uniform. The IV curves and the voltage required to yield 20  $\mu$ A of output current are consistent with the observed emission behavior on cycling (Figure 10.7e).

Demonstration of mechanical stability and electrical reliability under complex loading conditions provides further evidence of the effectiveness of these design strategies. Balloon inflation induces a bi-axial stretching mode. Figure 10.8a shows images of an array of  $\mu$ -ILEDs transformed from a flat geometry to a hemispherical balloon shape (left frame) by injecting air into an underlying cavity, along with magnified views collected from the top (right frame). An areal expansion of 70% in this case does not induce any breakage in the devices or change in the emission strength. The IV curves in Figure 10.8b verify that there is no appreciable difference during balloon inflation and deflation (Figure 10.8c). Twisting of rubber band type substrates creates a distributed, 3D loading of the structure (Figure 10.8d). Rotations of  $360^\circ$  and  $720^\circ$  show no noticeable mechanical damage or change in light emission, as confirmed by bright (left, with external illumination) and dark (right, without external illumination) images of Figure 10.8e. Out-of-plane buckling, rotation, and twisting of weakly bonded serpentine bridges accommodate most of the applied deformation (Figure 10.8e, SEM image for  $360^\circ$  twisting), enabling reliable electrical operation (Figure 10.8f) under extreme loading conditions (Figure 10.8g).

### 10.3.2

#### Lighting Devices on Substrates of Unconventional Materials and Shapes

As with electronics, the design strategies described above enable  $\mu$ -ILEDs to be integrated onto diverse substrate types including fabrics, fallen leaves, paper, and aluminum foil, as explicitly demonstrated [33]. Figure 10.9a and b show arrays of  $\mu$ -ILEDs on a paper substrate folded twice and a similar array on a crumpled piece of aluminum foil, respectively. In both cases of extreme deformations, no change

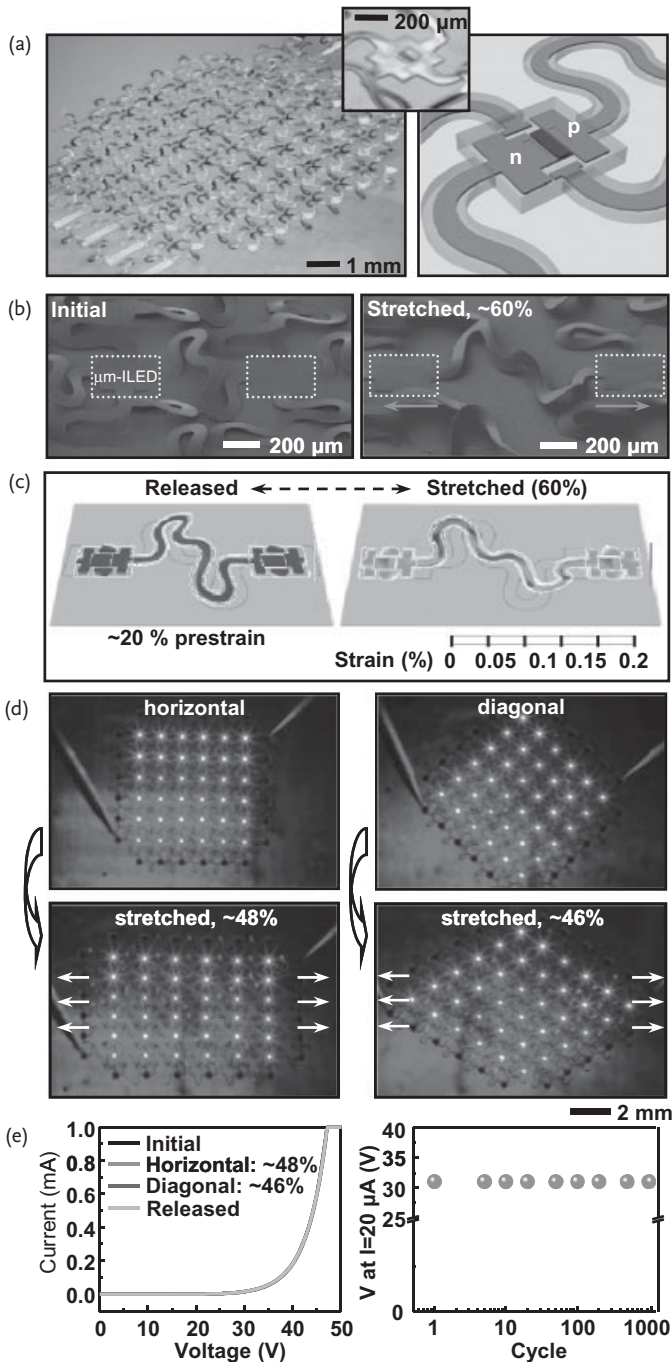


**Figure 10.7** (a) Image of a  $6 \times 6$   $\mu\text{-ILED}$  array with serpentine interconnects on a glass substrate (left) and a schematic illustration of a single pixel (right frame). The inset shows a magnified image of a single pixel. (b) SEM images of two  $\mu\text{-ILED}$ s connected by noncoplanar serpentine interconnects before (left) and after (right) stretching. (c) FEM strain distribution before (left) and after

(right) stretching. (d) Images of a stretchable  $6 \times 6$   $\mu\text{-ILED}$  array under different applied strain (top left: 0%, bottom left: 48% along x direction, top right: 0%, bottom right: 46% along diagonal direction). (e) Current-voltage characteristics of a  $6 \times 6$   $\mu\text{-ILED}$  array under different applied strain (left) and voltage at the current of 20 mA for each stretching cycle (48% applied strain along the x direction, right).

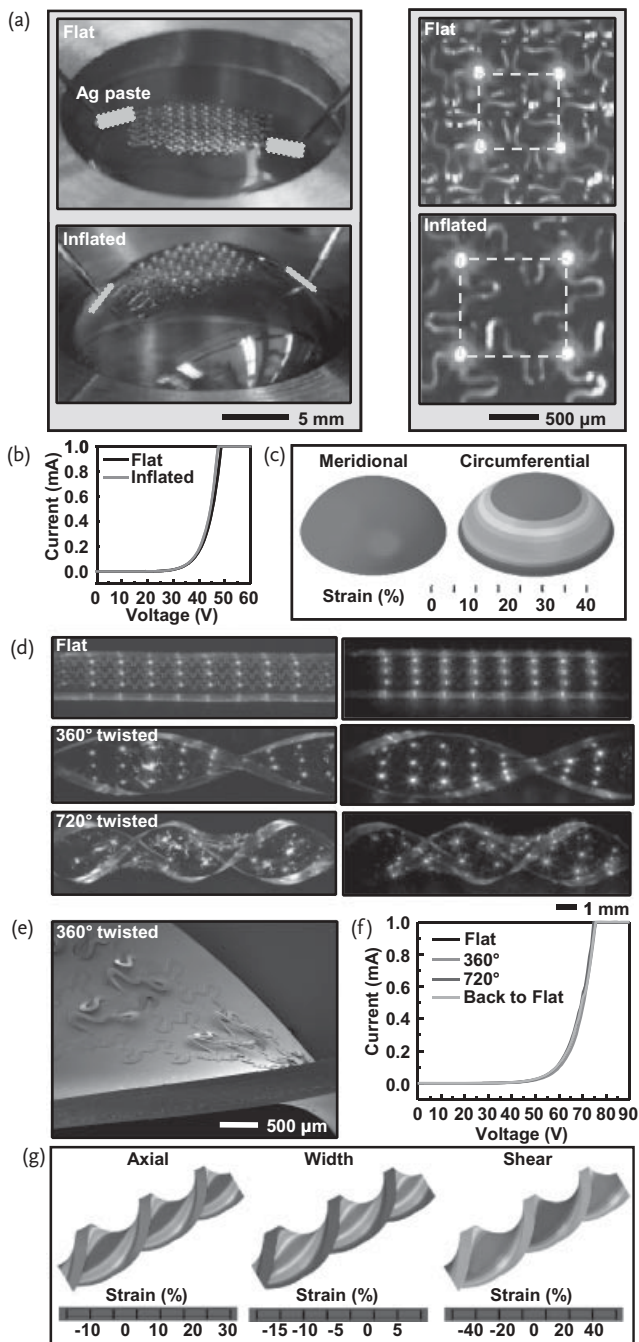


**Figure 10.8** (a) Images of balloon deformation of a stretchable  $6 \times 6$   $\mu$ -LED array (left). The right frame gives a magnified view from the top, which shows the area expansion during stretching. (b) Current–voltage characteristic in the flat and inflated states. (c) FEM simulation of strain distributions induced during balloon stretching. (d) Images of a  $3 \times 8$   $\mu$ -LED array on a thin PDMS substrate at different degrees of twisting. The

top frame shows a normal state and the middle and bottom frames show  $360^\circ$  and  $720^\circ$  twists with (left) and without (right) external illumination. (e) SEM image of an  $\mu$ -LED array under  $360^\circ$  twisting. (f) Current–voltage characteristics under different degree of twisting ( $0^\circ$ ,  $360^\circ$ , and  $720^\circ$ ). (g) FEM simulation of strain induced by twisting.

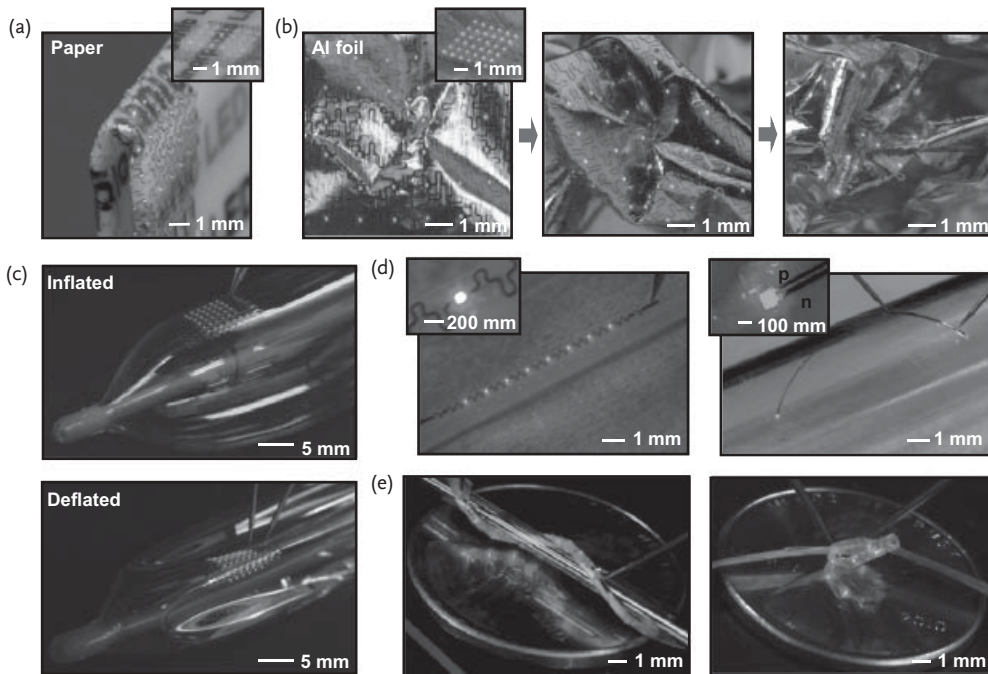


**Figure 10.9** (a) Image of a folded  $6 \times 6$   $\mu$ -ILED array on a paper substrate. The inset shows the normal state, before folding. (b) Images of a crumpled  $6 \times 6$   $\mu$ -ILED array on a piece of aluminum foil. The inset shows a flat array before crumpling. (c) Image of a  $6 \times 6$   $\mu$ -ILED array on a balloon catheter, in inflated (top) and deflated (bottom) states.

(d) Image of  $1 \times 8$   $\mu$ -ILED array on a plastic tube (left) and a single  $\mu$ -ILED on a thread wrapped around a glass cylinder (right). The insets show magnified views for a single pixel. (e) Image of  $1 \times 8$   $\mu$ -ILED array on  $\sim 0.7$  mm diameter thread wrapped around a glass rod (left) and in a knotted state (right).

in emission properties is observed. Arrays of  $\mu$ -ILEDs can be also transfer printed onto curvilinear surfaces. Examples include catheters, tubes, and threads, which can be utilized for biomedical applications [33]. Figure 10.9c shows an array on cylindrical balloon catheter. This inflatable catheter can be used for angioplasty, which involves compression of stenotic blood vessels, and for other surgical purposes.  $\mu$ -ILEDs might be used, in this case, for photodynamic therapy or for activation of photosensitized drugs, or for optical characterization of the tissue. Devices can even be transfer printed onto thin tubes or threads (Figure 10.9d and e). Serpentine interconnects provide levels of deformability necessary for wrapping or knotting of the tubes and threads. Other examples of related applications appear in the following sections on biomedical devices.

## 10.4

### Biomedical Applications of Stretchable Electronics and Optoelectronics

#### 10.4.1

##### Encapsulation Strategy

Bio-integrated electronics are, by definition, in close contact with biological tissues and, as such, they are exposed to, and often completely immersed in, biofluids [36]. As a result, a waterproof, insulating passivation layer is required to control the electrical points of contact [35–37]. Such layers not only protect the tissue from electrical shock but they also shield the electronics from fluids and ions, which can have major detrimental effects on the operation. Unwanted mechanical contact and abrasion during use can also cause device failure, in the absence of suitable protective coatings. The mechanical effects of such materials must, however, be carefully considered. For example, a typical formulation of PDMS (with a modulus of 2MPa) when used for encapsulation decreases the stretchability of an unencapsulated noncoplanar serpentine by up to ~50%. Such mechanical constraint can be tuned by changing the modulus of the encapsulation material [65]. Figure 10.10a shows a CMOS inverter with a straight pop-up bridge, encapsulated by PDMS of different moduli. The left frame shows the control case, without encapsulation layer. The center and right frames correspond to devices encapsulated by 0.1MPa and 1.8MPa PDMS, respectively. After encapsulation, each sample is stretched to the point of mechanical failure of the interconnection metal, as shown in the bottom frames of Figure 10.10a. With a ~60% prestrain, the device with no encapsulation can be stretched up to ~59% without mechanical fracture. However, for the case of encapsulated devices with PDMS of 0.1 and 1.8MPa modulus, the maximum stretchability just before the point of crack formation is decreased to ~55% and ~49%, respectively (Figure 10.10a). As the modulus of encapsulation material further decreases, more stretchability can be retained. This experimental observation is confirmed with the theoretical estimation using analytical model and numerical calculation (FEM). Figure 10.10b compares amplitudes of the noncoplanar bridge at the point of crack formation (top frames and left bottom frame). Based on these results, the maximum stretchability can also be estimated (right bottom frame). Using this encapsulation strategy, and mechanics design tools, many applications under harsh environments become possible.

#### 10.4.2

##### Bio-applications of $\mu$ -ILEDs: Suture Threads and Proximity Sensors

Thin threads with integrated  $\mu$ -ILEDs, with an outer diameter of ~300  $\mu\text{m}$ , can be used as wound sutures as, for example, devices to provide photoradiation therapy for accelerated wound healing (Figure 10.11a) [33], or as components for performing spectroscopy on the tissue near the wound site. Conventional LED radiation

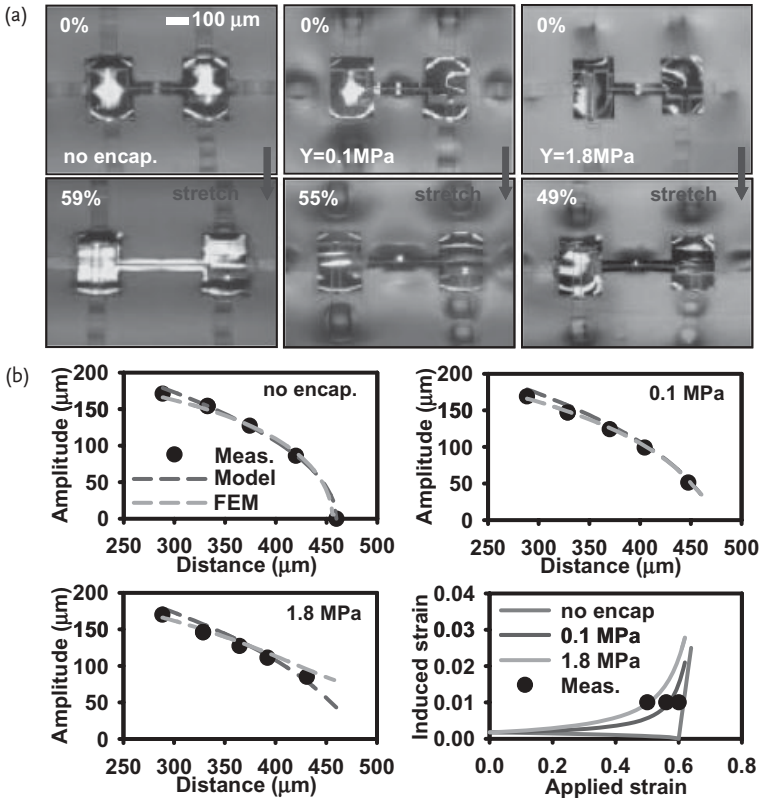
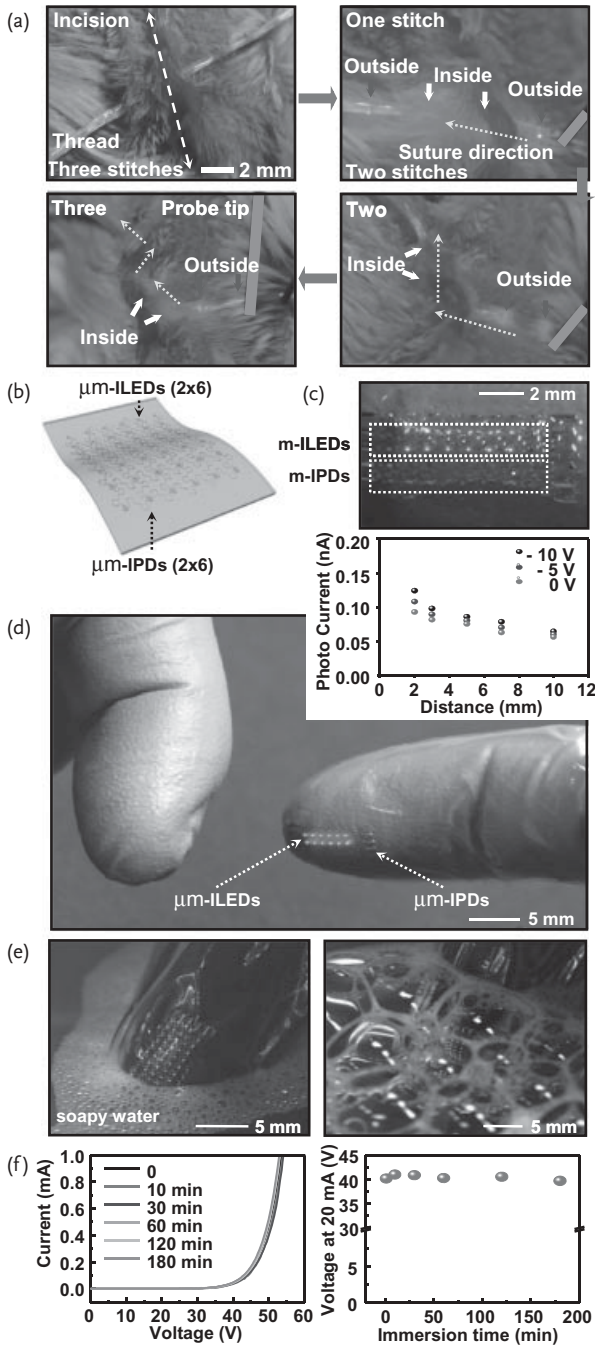


**Figure 10.10** (a) Optical microscope images of a stretchable inverter with straight noncoplanar interconnects at 0% strain (top) and at the maximum stretching state before visible cracking (bottom), for cases with no encapsulation (left), soft encapsulation (0.1 MPa, center), and hard encapsulation (1.8 MPa, right). (b) Amplitude of the noncoplanar interconnect as a function of

distance between two islands: measurements by experiments, estimations by analytical modeling, and FEM simulation for three different cases (no encapsulation, 0.1 MPa encapsulation, 1.8 MPa encapsulation). The right bottom frame shows the relationship between induced strain and applied strain for each encapsulation case.

**Figure 10.11** (a) Image of suture thread with a  $1 \times 4$  array of  $\mu$ -ILEDs on an animal model (mouse). An incision is sutured by a  $\mu$ -ILED thread: one stitch (left top,  $\mu$ -ILEDs are off), one stitch (right top,  $\mu$ -ILEDs are on), two stitches (right bottom), and three stitches (left bottom). The dashed arrows show the suturing direction. (b) Schematic illustration of a  $2 \times 6$  array of  $\mu$ -ILED and a corresponding array of photodetectors for the proximity sensing. (c) Magnified view of Figure 10.11d

( $2 \times 6$  forward biased  $\mu$ -ILEDs for light emission and  $2 \times 6$  reverse biased devices for photodetection) (top). Measured photocurrent at different distances from an object and at three different biases (bottom). (d) Image of the proximity sensor on a finger tip of vinyl glove. (e) Images of waterproof demonstration. (f) Current–voltage curves and voltages at 20 mA current for different times for immersion in soapy water.



therapy uses external light sources, for which the light penetration efficiency into wounded tissue is limited, and the exposed regions are poorly defined. In contrast, a  $\mu$ -ILED suture thread can wrap the wounded area intimately, to maximize the absorption efficiency due to its proximity, as well as to spatially localize the exposed regions. Moreover, the  $360^\circ$  pattern of radiation toward the wound further increases the absorption efficiency. Figure 10.11a shows thin  $\mu$ -ILEDs suture thread used to close an incision in the dermis of an animal model (mouse). The various frames show the suturing process, stitch by stitch.

Addition of photodetectors to such a platform enables, in principle, spectroscopy for determining blood oxygenation or other key parameters of the tissue. Various scattering properties can also be determined. Reflections can be used to remotely sense the distance to an external object, which is a challenging problem in robotic control, particularly when the robot part is nonplanar and not easily amenable to the mounting of conventional, planar optoelectronics technologies. Proximity sensing on the surface of the fingertip of a glove can be achieved by integrated arrays of  $\mu$ -ILEDs and corresponding microscale photodiodes [33]. In this case,  $\mu$ -ILEDs are forward biased to convert electrical energy into light emission, while the same types of devices are reverse biased to collect photons and convert them into electrical current. By integrating these two oppositely biased arrays, i.e., a  $2 \times 6$  array of  $\mu$ -ILEDs and a  $2 \times 6$  array of photodiodes ( $\mu$ -IPDs), proximity sensing at finger tip can be achieved, as shown in Figure 10.11b and c. Here, the photodiodes collect backscattered or reflected light, emitted from the  $\mu$ -ILEDs and returned back by interaction with external objects. The bottom frame of Figure 10.11c shows the change in photocurrent at different distances between the sensor and object. Photocurrent also increases at higher biases applied to the photodiodes, as expected. For all cases, the arrays of  $\mu$ -ILEDs are operated at a constant current of 1 mA. Stretchable designs allow the system to be integrated onto unconventional surfaces, in this case the fingertip region of a glove (Figure 10.11d). In addition, a waterproof encapsulation technology involving coatings of PDMS enables the sensors to operate in soapy water without any mechanical or electrical degradation over long periods of time (Figure 10.11e and f).

#### 10.4.3

##### **Minimally Invasive Surgical Tools: Instrumented Balloon Catheters**

Cardiac arrhythmias, such as atrial fibrillation or ventricular tachycardia, are among the most severe types of cardiac disorders, often terminating in sudden death [71]. Common therapies involve either implantable pacemaker/defibrillator technologies or cryo/radio frequency (RF) ablation of targeted tissue as part of surgical operations [71]. Such ablation procedures require mapping of electrocardiography (ECG) over large areas of the heart to locate abnormal nodes that cause the arrhythmia, followed by precise delivery of energy to create lesions with desired shapes and depths, to eliminate the relevant part of the cardiac muscle [71]. For accurate control, high precision pressure and temperature sensing capabilities are required

to guide the ablation. In particular, pressure sensing can ensure direct mechanical contact between the ablaters and the endocardial/epicardial tissues; temperature is a valuable monitor of the extent of ablation.

In minimally invasive surgeries, a small incision is made at the thigh for the insertion of a thin and long catheter into veins to reach the diseased intravascular or endocardial regions [71]. The state-of-the-art minimally invasive surgery utilizes single-lead catheters for endocardial ECG sensing or RF ablation and passive balloon catheters as mechanical manipulators, as in angioplasty and septostomy [71]. The need for multiple catheterization, however, increases the time of the procedure and hence the risk of the patients. Multifunctional balloon catheters, with various kinds of sensors and stimulators, circumvent these problems [37]. As an example, we demonstrated an “instrumented” balloon catheter with capabilities of mapping, pacing, ablation, temperature recording, pressure sensing, and photodynamic therapy (Figure 10.12a and b). For a realistic balloon catheter (8–18 Fr, BARD, USA; Creganna, Ireland), huge expandability (beyond 100%) is required for easy insertion and later large inflation to achieve intimate contact with endocardial tissues. We adopted noncoplanar serpentine interconnects to achieve large stretchability, of up to ~130% (Figure 10.12a and b). A final waterproof encapsulation layer using a biocompatible elastomer over the ribbon cable prevents electrical leakage current.

Figure 10.12c–h show results of *in vivo* animal experiments (rabbit model) that demonstrate multifunctionality and performance of such instrumented balloon catheters. For these tests, due to small sizes of blood vessels in rabbits, the heart was surgically exposed through a longitudinal sternotomy and pericardiotomy to enable epicardial evaluation. To prevent drying of the exposed heart surface, saline solution was supplied periodically to rinse the tissue. A basic function is ECG mapping. By using a closely spaced pair of electrodes (~1 mm spacing), local ECG signals were measured from the right ventricle (RV) and left atrium (LA) in Figure 10.12c and d, respectively. Each potential recorded by a pair of electrodes was differentiated for the purpose of plotting. Distinct waveforms from the RV and LA can be clearly seen, which is an important criterion for differentiating various locations of the heart. After locating nodes for abnormal heart rhythms, RF energy can be delivered through electrodes to create lesions and thereby frustrate the propagation of abnormal waves. To achieve effective ablation, close contact between the inflated balloon electrodes and the soft cardiac tissues is required. Specialized tactile sensors, capable of measuring normal force with little sensitivity to deformation of the underlying balloon substrate, provide valuable functionality in this context. To demonstrate sensitivity, such devices were pressed against the outside of the beating heart, and the response was recorded (Figure 10.12e and f). To enable feedback control over the size and depth of the lesions formed by ablation, local temperature measurements can be useful. Devices for this purpose were evaluated, by extracting their response in synchrony with the delivery of RF power (Figure 10.12g and h). Such temperature recordings can be used to estimate lesion depth and area by use of theoretical models of heat flow [37].

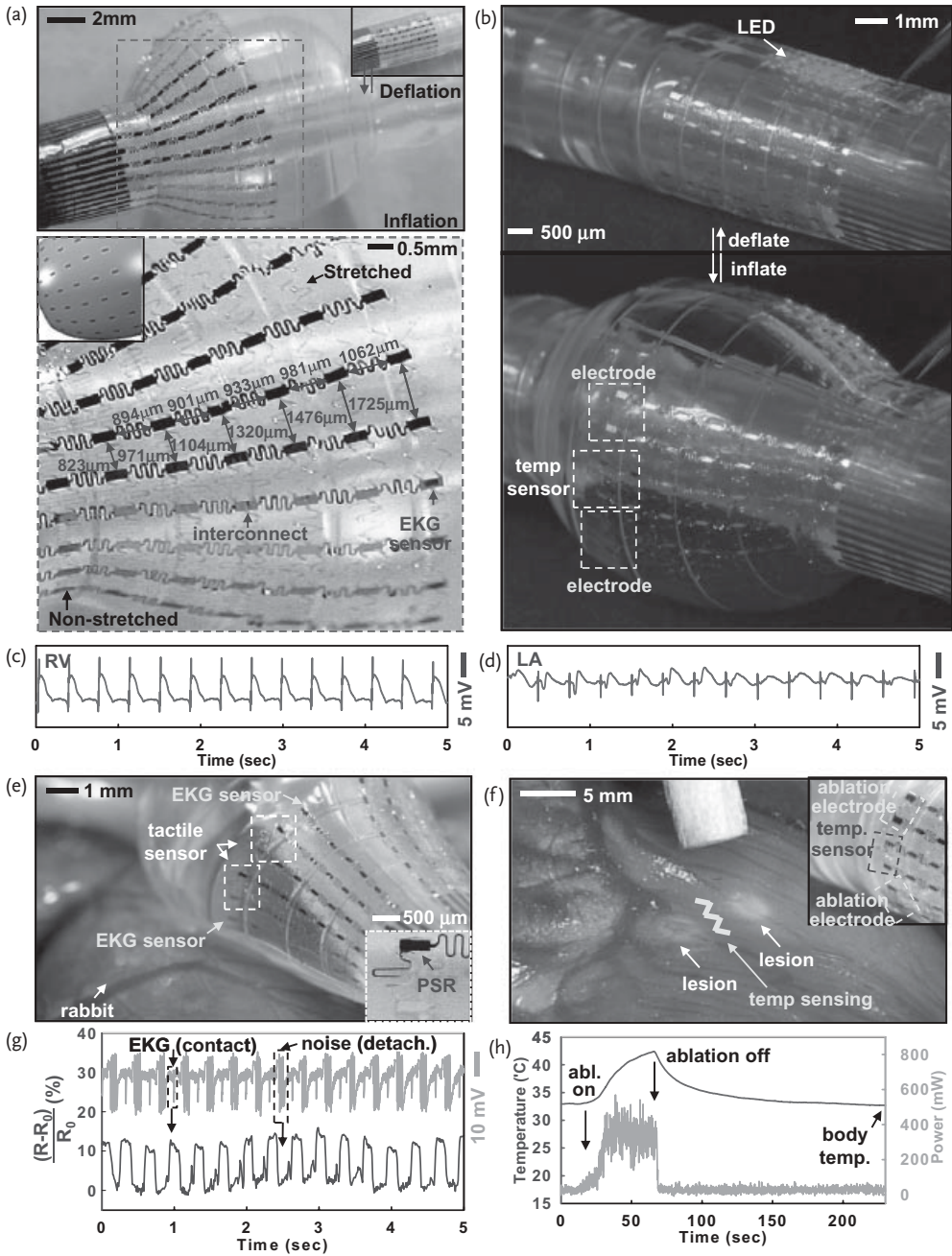


**Figure 10.12** (a) Image of an electrode array integrated onto a balloon catheter, and a magnified view in inflated and deflated states (top frame inset). The bottom frame inset shows the corresponding FEM simulation result. (b) Image of a multifunctional balloon catheter in deflated and inflated states. Electrocardiography (ECG) performed on the epicardial surface of the right ventricle (c) and left atrium (d). (e) Image of tactile sensors on an inflated balloon contacted to the epicardial surface. The inset shows a magnified view of a tactile sensor. (f) Simultaneous recording of ECG and pressure change during beating of the heart. (g) Image of lesion marks created by ablation electrodes that deliver RF energy to cardiac tissue. The zig-zag line denotes the location of the temperature sensor. The inset shows representative electrodes and a temperature sensor. (h) Temperature and power monitoring data. RF power and temperature are synchronized, as expected.



#### 10.4.4

##### Epidermal Electronic System (EES)

Monitoring and simulation via interfaces to the body through the skin have represented topics of long-standing interest [72, 73]. Examples include electrocardiography (ECG), electromyography (EMG), and electroencephalography (EEG), as well as temperature, motion, and location sensing. Transcutaneous electrical nerve stimulation (TENS) is a separate area of significance. Existing skin-mounted systems use point-contact electrodes, usually with bulk dimensions, that offer limited spatial resolution and use either adhesive tapes or conductive gels for good mechanical and electrical coupling [74]. Such setups can be valuable in certain settings, but they are not compatible with long-term measurements, due to skin irritation and drying of conductive gels [74]. The concepts of stretchable electronics, taken to an extreme, allow monitoring/stimulation systems to be constructed with thicknesses, Young's moduli, bending stiffnesses, and areal densities matched to the epidermis itself. These devices are able to form conformal contacts with the skin surface to achieve robust binding even without the use of adhesives. We refer to this type of technology as an "epidermal" electronic system (EES). Figure 10.13 shows an EES with ultrathin configuration, ultrasoft substrate, and mechanically optimized circuit layout, as an open mesh with devices and interconnects in filamentary serpentine shapes [38]. Figure 10.13a shows undeformed and deformed (under either compression or tension) epidermal electronics on human skin. Due to its mechanical properties, the EES confers minimal mechanical constraints on skin movement and remains in intimate contact with the skin even during stretching or wrinkling. EES can be built as highly integrated, multifunctional systems with electrophysiological, temperature and strain sensors, wireless power transmission coils, and building blocks for radio frequency (RF) communications. A commercial temporary transfer tattoo as a substrate, instead of a low modulus elastomer, represents another option in which the adhesives used in the tattoo can improve the robustness of bonding to the skin (Figure 10.13b). Application against the skin sandwiches the device between the skin surface and the temporary tattoo.

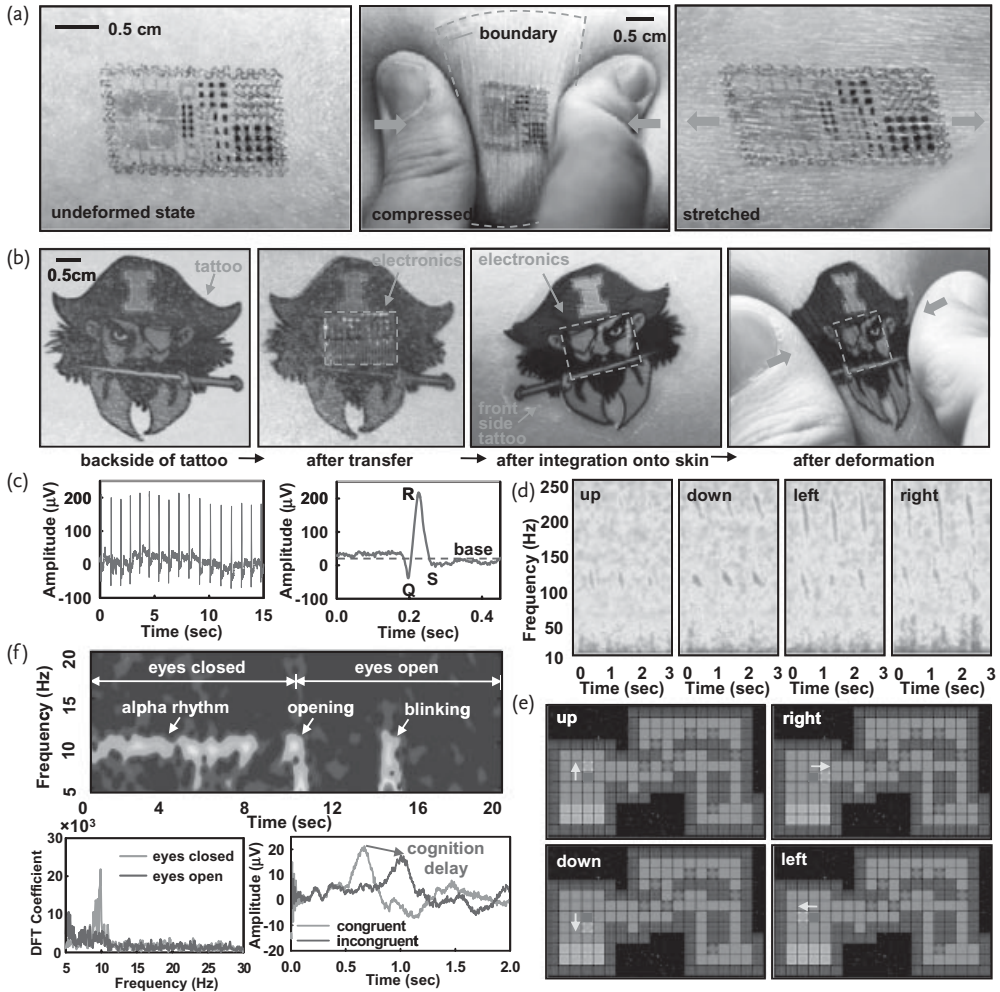


**Figure 10.13** (a) Schematic illustration and corresponding image of a tunable electronic eye camera. (b) Images of a detector array with tunable curvature in its flat state (top) and concave state (bottom), adjusted using hydraulic actuation. (c) Image of a fully integrated tunable electronic eye camera, including tunable fluidic lens and photodiode array, flexible wiring, and data cables. (d) Images of a test pattern consisting of an

array of dots, captured with a tunable electronic eye camera in its flat state (left) and in curved state (right). (e) Radius of curvature and focal distance of four different lenses (distances from the lens ( $z$ ): 16, 24, 38, and 55 mm, corresponding radii of curvature: 4.9, 6.1, 7.3, and 11.5 mm). (f) Images acquired by a complete camera system at four different lens conditions.

The whole system remains in conformal contact during skin deformation as shown in the last frame of Figure 10.13b.

Examples of real applications of EES appear in Figure 10.13c–e. Here, the EES mounts on various body parts, such as the chest, neck, and forehead to enable ECG, EMG, and EEG measurements, respectively. Figure 10.13c presents representative ECG data collected from the human chest, showing the different phases of a heart pulse (right frame of Figure 10.13c). As another demonstration, we recorded electrophysiological signals associated with muscle movements, EMG, from the neck (Figure 10.13d). These EMG signals were recorded when the subject was speaking four different words (“up,” “down,” “left,” and “right”), repeating 10 times each, at the speed of one word per second. The recorded data were plotted as spectrograms to compare frequency components and patterns for this speech. To illustrate the potential for use of such data in human–machine interface, we simulated gaming control by applying pattern recognition algorithms to the EMG data. The user controlled an avatar that can move in four directions in the game Sokoban, using neck EMG (Figure 10.13e). Interfaces to prosthetics represent other potential opportunities with significance to human health.

As another example, we recorded EEG from the forehead to show capabilities for observing alpha rhythms on subjects with their eyes open and closed. The measurements confirm well-known phenomena involving strong alpha rhythms with frequencies around 10 Hz from the occipital area when the eyes are closed (top and left bottom frame of Figure 10.13f) and absence of this activity with the eyes open. The signal-to-noise ratios exhibited here are comparable to those obtained in otherwise identical experiments with conventional electrodes that require electrically conducting gels. Another experiment in recognizing colored words in congruent and incongruent cases (Stroop test) was performed [75]. When the word color matches with the real color, the recognition was faster than unmatched case. The cognition delay compared to an unmatched case is shown in right bottom frame of Figure 10.13f.

## 10.5 Stretchable Digital Imagers and Solar Modules

### 10.5.1 Hemispherical Electronic Eye Camera

In addition to devices that integrate with biology, stretchable electronics open up opportunities for engineering concepts that draw inspiration from biology. An example is in digital cameras. Conventional devices use planar arrays of photodetectors, coupled with multicomponent imaging optics, to generate images with matching, planar geometries. Biology, as evidenced by the mammalian eye, uses, instead, curved photodetector arrays and relatively simple optics. Curvature can be important in this context because it allows the geometry of the detector array

to match that of the image surface that forms when, for example, a single plano-convex lens is used for imaging. For man-made systems, the challenge is in adopting semiconductor processing technologies, which are all well developed only for use on the extremely flat surfaces of semiconductor wafers or plates of glass, for fabricating devices on surfaces with hemispherical shapes or other curvature. The concepts of stretchable electronics bypass these challenges by enabling the formation of photodetector arrays on planar surfaces, followed by their geometrical transformation into curved surfaces. This transformation is possible only with systems that can accommodate large strain deformations. Theoretical modeling reveals the detailed mechanics associated with such a process, including strain distributions and locations of each pixel as the transformation occurs. An example for the case of a  $16 \times 16$  array of silicon photodiodes appears in Figure 10.14a [41].

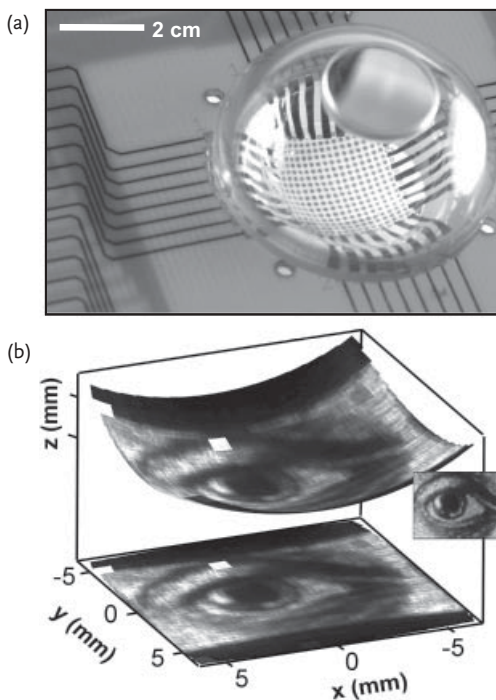


**Figure 10.14** (a) Epidermal electronic device mounted on the skin: undeformed state (left), under compressive strain (middle frame), and under tensile strain (right frame). (b) A backside image of a commercial temporary tattoo (first frame), electrode array transfer-printed on the tattoo (second frame), after applied to the skin (third frame) and under compressive strain (fourth frame). (c) ECG measurement with an epidermal electronic

device (left frame) and magnified view of the recording of a single heartbeat (right frame). (d) Spectrogram of EMG measurement from the neck for four different voice commands, “up,” “down,” “left,” and “right.” (e) Video game control using recorded EMG signals. (f) Alpha rhythm measurement, spectrogram (top) and plots after Fourier transformation (left bottom). Right bottom frame shows Stroop test results.

A single unit cell consists of a silicon photodiode and a blocking diode to enable passive matrix addressing. This system, connected using stretchable designs described previously, can be wrapped onto hemispherical surfaces by use of non-coplanar structures and ultrathin NMP designs to minimize induced strains in the devices and active materials. This hemispherical detector can be integrated with a printed circuit board (Figure 10.14a) to provide connection to external data acquisition systems, thereby yielding a functioning camera that is capable of taking pictures. This design offers several benefits, such as large field of view, excellent illumination uniformity, and low aberrations, compared with a planar imaging device when similarly simple imaging optics are used. In the case of the hemispherical camera described here, a single element plano-convex lens provides this functionality. The image in this case has, more accurately, the shape of an elliptic paraboloid (known as the Petzval surface), which is approximated by the hemispherical shape of the detector. Figure 10.14b shows comparisons between imaging on a hemispherical surface (top) and planar surface projection (bottom), for this case. The small inset shows the original image.

### 10.5.2

#### **Curvilinear Imagers and Stretchable Photovoltaic Modules with High Fill Factors**

One deficiency of the photodetector design described above is that the noncoplanar interconnects occupy space that could otherwise be filled with additional detector area. A goal is to optimize the fill-factor associated with the photodetectors, while retaining sufficient stretchability to accomplish the geometry transformation. Similar considerations are relevant to other devices that benefit from high area coverage of active devices, ranging from photovoltaic modules to lighting systems [33, 76]. Two approaches can be implemented to address this issue. The first involves the clustering of multiple active elements per “island” in the mesh layout, together with a positioning of interconnects to span outer (rather than inner) edges of adjacent islands [43]. Figure 10.15a and b show SEM images of four clustered photodetectors in one island and its magnified image, respectively. This strategy successfully increases the fill-factor, while maintaining the deformability needed to achieve a hemispherical shape; quantitative analysis appears elsewhere [43]. The second concept exploits relief structures in the supporting substrate to isolate further device islands from applied strains and minimize the lengths of the interconnects [76]. Figure 10.15c and d shows such a layout. Here, active devices (solar cells in this particular case) are located at the thick, raised regions; metal wiring connects buckle downward into thin, recessed area in between the raised islands. Due to the thickness (height) difference, most of the applied strains localize in the recessed regions. As shown in Figure 10.15c, 123% strain is induced in thin bridge region, while only 0.4% strain is generated in thick island region for the overall strain of 20%. The results match FEM simulations shown in the bottom frame of Figure 10.15c. Images of a solar module that uses this strategy appears in Figure 10.15d. Even with short interconnects, and correspondingly large fill-factor, a significant amount of stretching and deformation is possible.

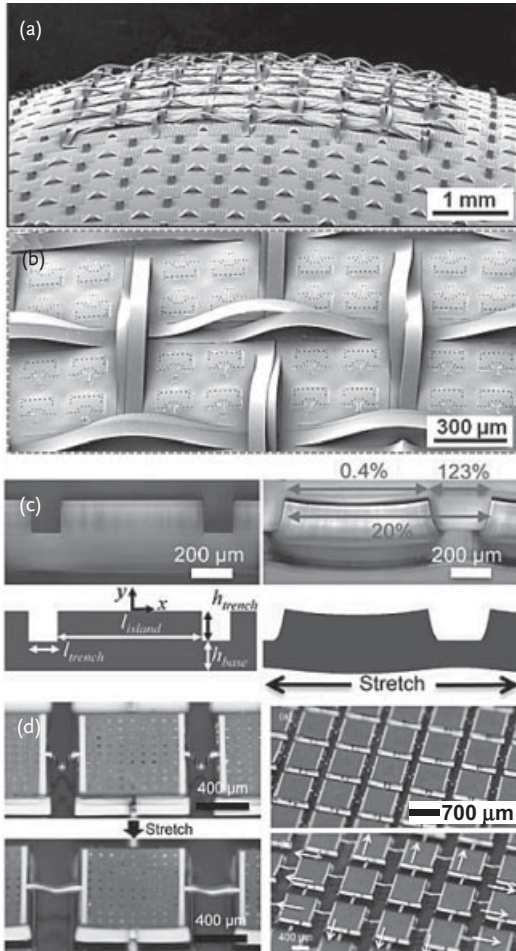


**Figure 10.15** (a) Image of a hemispherical detector array for an electronic eye camera, mounted on a printed circuit board. External connection through a flexible cable transfers measured data to a data acquisition system.

(b) Image of an eye (inset shows the raw printed image), captured by a hemispherical electronic eye camera (top), and its planar projection (bottom).

### 10.5.3

#### Hemispherical Electronic Eye Camera with Adjustable Zoom Magnification

One drawback of the cameras described in the previous sections is that, as in biological systems, the curvature of the detector cannot change significantly. As a result, the use of zoom lenses is impossible, because the magnification settings change the Petzval surface curvature in ways that lead to mismatches in shape with the detector. A solution exploits the concepts of stretchable electronics to

tune, reversibly, the curvature of a hemispherical photodetector array in a coordinated manner with the zoom lenses [42]. Figure 10.16a shows a schematic diagram and corresponding image of such a tunable electronic eye system. For tuning, the stretchable photodiode array bonds to a thin elastomeric (PDMS) membrane, whose curvature can be adjusted by applying pressure through a sealed fluidic chamber underneath the membrane. Depending on the setting of a tunable, fluidic plano-convex imaging lens, hydraulic actuation controls the radius of curvature of the photodiode array in an appropriate way, from a completely flat state to highly curvilinear hemispherical surface (Figure 10.16b). The design of each unit cell is the same as previous electronic eye systems. However, instead of straight interconnects, serpentine shapes were used to maximize the stretchability and reduce the mechanical strain effect on electrical performance of the photodiode array during actuation.

Figure 10.16c shows a completely wired version of this type of tunable electronic eye camera. Imaging demonstrations using test patterns of dots appear in Figure 10.16d, in which the imaging quality is compared to a planar detector array. While the periphery region shows similarly good image quality, a clear difference can be observed in the center region. The hemispherical array yields much higher fidelity due to a curvilinear shape that matches the Petzval surface. Similar experiments using a tunable electronic eye system are performed using four different magnification settings of a fluidic plano-convex lens (Figure 10.16e). Each lens configuration demands a different radius of curvature in the detector array for optimal quality in imaging (Figure 10.16f).

## 10.6 Conclusions

In conclusion, this chapter presents a few methods to use high-quality single crystal inorganic materials in stretchable electronic/optoelectronic systems. As reported in other chapters, alternative approaches, some of which rely on different classes of materials, are also under development and have recently shown great promise. A likely scenario is that different technologies can address different types of applications, in a complementary way. We find applications in bio-inspired device design and bio-integrated electronics to be most compelling, but many other possibilities also exist. The rich range of topics in both basic and applied science, and the strong potential for meaningful technologies, will create interest in this field for many years to come.

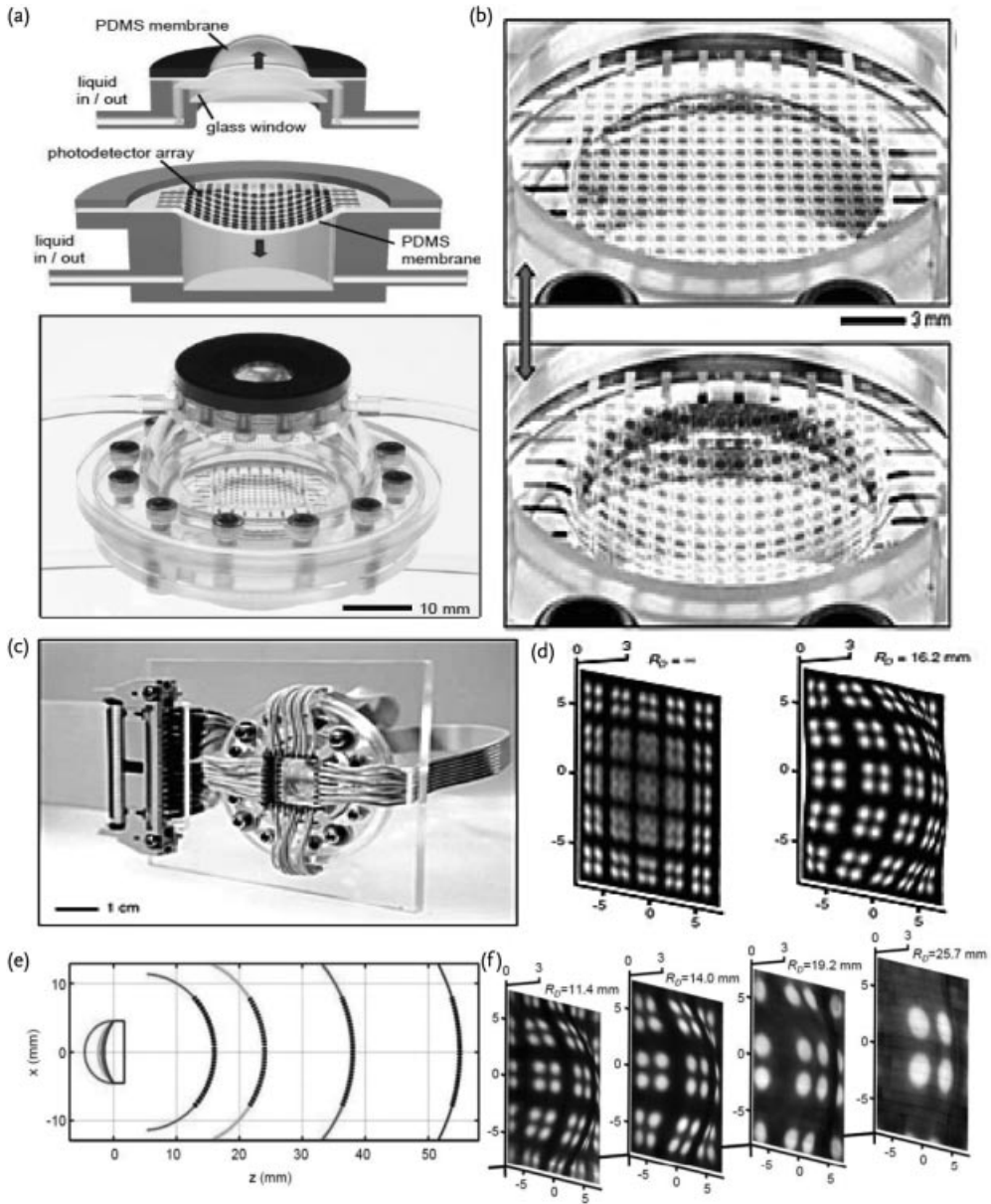


**Figure 10.16** SEM image of a photodiode array in a tiled configuration on a hemispherical substrate (a) and its magnified view (b). (c) Cross-sectional optical microscopy images (top) and corresponding FEM

simulation results (bottom) in normal (left) and stretched (right, ~20%) states, respectively. (d) Image of GaAs photodiode array before (top) and after (bottom) stretching (~20%, biaxial).

## References

- 1 Moore, G. (1965) *Electronics*, **38**, 114.
- 2 Arns, R.G. (1998) *Eng. Sci. Edu. J.*, **7**, 233.
- 3 Vogel, E.M. (2007) *Nat. Nanotech.*, **2**, 25.
- 4 International Roadmap Committee (2012) International Technology Roadmap for Semiconductors, www.itrs.net (accessed 25 September 2012).
- 5 Streetman, B.G., and Banerjee, S.K. (1981) *Solid State Electronic Devices*, 6th edn, Pearson, New Jersey.
- 6 Hayashi, I. (1993) *Jpn. J. Appl. Phys.*, **32**, 266.
- 7 Mishra, U.K., Shen, L., Kazior, T.E., and Wu, Y.-F. (2007) *Proc. IEEE*, **96**, 287.
- 8 Cantatore, E., Geuns, T.C.T., Gelinck, G.H., Veenendaal, E., Gruijthuisen, A.F.A., Schrijnemakers, L., Drews, S., and Leeuw, D.M. (2007) *IEEE J. Solid-St. Circ.*, **42**, 84.
- 9 Bettinger, C., and Bao, Z. (2010) *Adv. Mater.*, **22**, 651.
- 10 Sekitani, T., Noguchi, Y., Zschieschang, U., Klauk, H., and Someya, T. (2008) *Proc. Natl. Acad. Sci. USA*, **105**, 4979.
- 11 Kuik, M., Nicolai, H.T., Lenes, M., Wetzelaer, G.-J.A.H., Lu, M., and Blom, P.W.M. (2011) *Appl. Phys. Lett.*, **98**, 093301.
- 12 Forrest, S.R. (2004) *Nature*, **428**, 911.
- 13 Rogers, J.A., Bao, Z., Baldwin, K., Dodabalapur, A., Crone, B., Raju, V.R., Kuck, V., Katz, H., Amundson, K., Ewing, J., and Drzaic, P. (2001) *Proc. Natl. Acad. Sci. USA*, **9**, 4835.
- 14 Someya, T., Kato, Y., Sekitani, T., Lba, S., Noguchi, Y., Murase, Y., Kawaguchi, H., and Sakurai, T. (2005) *Proc. Natl. Acad. Sci. USA*, **102**, 12321.
- 15 Ouyang, J., Chu, C.-W., Szmanda, C.R., Ma, L., and Yang, Y. (2004) *Nat. Mater.*, **3**, 918.
- 16 Yu, G., Gao, J., Hummelen, J.C., Wudi, F., and Heeger, A.J. (1995) *Science*, **270**, 1789.
- 17 Gelinck, G.H., Huitema, H.E.A., Veenendaal, E.V., Cantatore, E., Schrijnemakers, L., van der Putten, J.B.P.H., Geuns, T.C.T., Beenhakkers, M., Giesbers, J.B., Huisman, B.-H., Meijer, E.J., Benito, E.M., Touwslager, F.J., Marsman, A.W., van Rens, B.J.E., and de Leeuw, D.M. (2004) *Nat. Mater.*, **3**, 106.
- 18 Lipomi, D.J., and Bao, Z. (2011) *Energy Environ. Sci.*, **4**, 3314.
- 19 Jain, K., Klosner, M., Zemel, M., and Raghunandan, S. (2005) *Proc. IEEE*, **93**, 1500.
- 20 Huitema, H.E.A., Gelinck, G.H., van der Putten, J.B.P.H., Kuijk, K.E., Hart, C.M., Cantatore, E., Herwig, P.T., van Breemen, A.J.J.M., and de Leeuw, D.M. (2001) *Nature*, **414**, 599.
- 21 Kim, D.-H., Xiao, J., Song, J., Huang, Y., and Rogers, J.A. (2010) *Adv. Mater.*, **22**, 2108.
- 22 Reuss, R.H., Chalamala, B.R., Moussessian, A., Kane, M.G., Kumar, A., Zhang, D.C., Rogers, J.A., Hatalis, M., Temple, D., Moddel, G., Eliasson, B.J., Estes, M.J., Kunze, J., Handy, E.S., Harmon, E.S., Salzman, D.B., Woodall, J.M., Alam, M.A., Murthy, J.Y., Jacobsen, S.C., Olivier, M., Markus, D., Campbell, P.M., and Snow, E. *Proc. IEEE*, **93**, 1239 (2005).
- 23 Cao, Q., Kim, H.-S., Pimparkar, N., Kulkarni, J.P., Wang, C., Shim, M., Roy, K., Alam, M.A., and Rogers, J.A. (2008) *Nature*, **454**, 495.
- 24 Kocabas, C., Kim, H.-S., Banks, T., Rogers, J.A., Pesetski, A.A., Baumgardner, J.E., Krishnaswamy, S.V., and Zhang, H. (2008) *Proc. Natl. Acad. Sci. USA*, **105**, 1405.
- 25 Kim, K.S., Zhao, Y., Jang, H., Lee, S.Y., Kim, J.M., Kim, K.S., Ahn, J.-H., Kim, P., Choi, J.-Y., and Hong, B.H. (2009) *Nature*, **457**, 706.
- 26 McAlpine, M.C., Ahmad, H., Wang, D., and Heath, J.R. (2007) *Nat. Mater.*, **6**, 379.
- 27 Friedman, R.S., McAlpine, M.C., Ricketts, D.S., Ham, D., and Lieber, C.M. (2005) *Nature*, **434**, 1085.
- 28 Khang, D.Y., Jiang, H., Huang, Y., and Rogers, J.A. (2006) *Science*, **311**, 208.
- 29 Kim, D.-H., Ahn, J.-H., Kim, H.-S., Lee, K.J., Kim, T.-H., Yu, C.-J., Nuzzo, R.G., and Rogers, J.A. (2008) *IEEE Electron. Device Lett.*, **29**, 73.

- 30 Choi, W.M., Song, J., Khang, D.-Y., Jiang, H., Huang, Y.Y., and Rogers, J.A. (2007) *Nano Lett.*, **7**, 1655.
- 31 Kim, D.-H., Ahn, J.-H., Choi, W.M., Kim, H.-S., Kim, T.-H., Song, J., Huang, Y.Y., Liu, Z., Lu, C., and Rogers, J.A. (2008) *Science*, **320**, 507.
- 32 Kim, D.-H., Song, J., Choi, W.M., Kim, H.-S., Kim, R.-H., Liu, Z., Huang, Y.Y., Hwang, K.-C., Zhang, Y.-W., and Rogers, J.A. (2008) *Proc. Natl. Acad. Sci. USA*, **105**, 18675.
- 33 Kim, R.-H., Kim, D.-H., Xiao, J., Kim, B.H., Park, S.-I., Panilaitis, B., Ghaffari, R., Yao, J., Li, M., Liu, Z., Malyarchuk, V., Kim, D.G., Le, A.-P., Nuzzo, R.G., Kaplan, D.L., Omenetto, F.G., Huang, Y., Kang, Z., and Rogers, J.A. (2010) *Nat. Mater.*, **9**, 929.
- 34 Park, S.-I., Le, A.-P., Wu, J., Huang, Y., Li, X., and Rogers, J.A. (2010) *Adv. Mater.*, **22**, 3062.
- 35 Kim, D.-H., Viventi, J., Amsden, J.J., Xiao, J., Vigeland, L., Kim, Y.-S., Blanco, J.A., Panilaitis, B., Frechette, E.S., Contreras, D., Kaplan, D.L., Omenetto, F.G., Huang, Y., Hwang, K.-C., Zakin, M.R., Litt, B., and Rogers, J.A. (2010) *Nat. Mater.*, **9**, 511.
- 36 Viventi, J., Kim, D.-H., Moss, J.D., Kim, Y.-S., Blanco, J.A., Annetta, N., Hicks, A., Xiao, J., Huang, Y., Callans, D.J., Rogers, J.A., and Litt, B. (2010) *Sci. Trans. Med.*, **2**, 24ra22.
- 37 Kim, D.-H., Lu, N., Ghaffari, R., Kim, Y.-S., Lee, S.P., Xu, L., Wu, J., Kim, R.-H., Song, J., Liu, Z., Viventi, J., Graff, B.D., Elolampi, B., Mansour, M., Slepian, M.J., Hwang, S., Moss, J.D., Won, S.-M., Huang, Y., Litt, B., and Rogers, J.A. (2011) *Nat. Mater.*, **10**, 316.
- 38 Kim, D.-H., Lu, N., Ma, R., Kim, Y.-S., Kim, R.-H., Wang, S., Wu, J., Won, S.M., Tao, H., Islam, A., Yu, K.J., Kim, T.-I., Chowdhury, R., Ying, M., Xu, L., Li, M., Chung, H.-J., Keum, H., McCormick, M., Liu, P., Zhang, Y.-W., Omenetto, F.G., Huang, Y., Coleman, T., and Rogers, J.A. (2011) *Science*, **333**, 838.
- 39 Lacour, S.P., Tsay, C., Wagner, S., Yu, Z., and Morrison, B., III (2005) in *IEEE Sensors 2005*, IEEE, p. 4.
- 40 Graudejus, O., Yu, Z., Jones, J., Morrison, B., III, and Wagner, S. (2009) *J. Electrochem. Soc.*, **156**, 85.
- 41 Ko, H.C., Stoykovich, M.P., Song, J., Malyarchuk, V., Choi, W.M., Yu, C.-J., Geddes, J., III, Xiao, J., Wang, S., Huang, Y.Y., and Rogers, J.A. (2008) *Nature*, **454**, 748.
- 42 Jung, I., Xiao, J., Malyarchuk, V., Lu, C., Li, M., Liu, Z., Yoon, J., Huang, Y., and Rogers, J.A. (2011) *Proc. Natl. Acad. Sci. USA*, **108**, 1788.
- 43 Shin, G., Jung, I., Malyarchuk, V., Song, J., Wang, S., Ko, H.C., Huang, Y., Ha, J.S., and Rogers, J.A. (2010) *Small*, **6**, 851.
- 44 Jung, I., Shin, G., Malyarchuk, V., Ha, J.S., and Rogers, J.A. (2010) *Appl. Phys. Lett.*, **96**, 021110.
- 45 Jiang, H., Khang, D.-Y., Song, J., Sun, Y., Huang, Y.Y., and Rogers, J.A. (2007) *Proc. Natl. Acad. Sci. USA*, **104**, 15607.
- 46 Song, J., Jiang, H., Choi, W.M., Khang, D.Y., Huang, Y., and Rogers, J.A. (2008) *J. Appl. Phys.*, **103**, 014303.
- 47 Sun, Y., Choi, W.M., Jiang, H., Huang, Y., and Rogers, J.A. (2006) *Nat. Nanotechnol.*, **1**, 201.
- 48 Gray, D.S., Tien, J., and Chen, C.S. (2004) *Adv. Mater.*, **16**, 393.
- 49 Bowden, N., Brittain, S., Evans, A.G., Hutchinson, J.W., and Whitesides, G.M. (1998) *Nature*, **393**, 146.
- 50 Lacour, S.P., Jones, J., Suo, Z., and Wagner, S. (2004) *IEEE Electron. Device Lett.*, **25**, 179.
- 51 Lacour, S.P., Jones, J., Wagner, S., Li, T., and Suo, Z. *Proc. IEEE*, **93**, 1459 (2005).
- 52 Lacour, S.P., Chan, D., Wagner, S., Li, T., and Suo, Z. (2006) *Appl. Phys. Lett.*, **88**, 204103.
- 53 Brosteaux, D., Axisa, F., Gonzalez, M., and Vanfleteren, J. (2007) *IEEE Electron. Device Lett.*, **28**, 552.
- 54 Gonzalez, M., Axisa, F., Bulcke, M.V., Brosteaux, D., Vandeveld, B., and Vanfleteren, J. (2008) *Microelectron. Reliab.*, **48**, 825.
- 55 Huyghe, B., Rogier, H., Vanfleteren, J., and Axisa, F. (2008) *IEEE Trans. Adv. Packaging*, **31**, 802.
- 56 da Silva, V.D. (2005) *Mechanics and Strength of Materials*, Springer, New York.

- 57 Patolsky, F., Zheng, G., and Lieber, C.M. (2006) *Nat. Protocol*, **1**, 1711.
- 58 Kong, X.Y., Ding, Y., Yang, R.S., and Wang, Z.L. (2004) *Science*, **303**, 1348.
- 59 Mack, S., Meitl, M.A., Baca, A.J., Zhu, Z.-T., and Rogers, J.A. (2006) *Appl. Phys. Lett.*, **88**, 213101.
- 60 Baca, A.J., Meitl, M.A., Ko, H.C., Mack, S., Kim, H.-S., Dong, J., Ferreira, P.M., and Rogers, J.A. (2007) *Adv. Func. Mater.*, **17**, 3051.
- 61 Ko, H.C., Baca, A.J., and Rogers, J.A. (2006) *Nano Lett.*, **6**, 2318.
- 62 Sun, Y., Khang, D.-Y., Hua, F., Hurley, K., Nuzzo, R.G., and Rogers, J.A. (2005) *Adv. Func. Mater.*, **15**, 30.
- 63 Chung, H.-J., Kim, T.-I., Kim, H.-S., Wells, S.A., Jo, S., Ahmed, N., Jung, Y.H., Won, S.M., Bower, C.A., and Rogers, J.A. (2011) *Adv. Funct. Mater.*, **21**, 3029.
- 64 Meitl, M.A., Zhu, Z.-T., Kumar, V., Lee, K.J., Feng, X., Huang, Y.Y., Adesida, I., Nuzzo, R.G., and Rogers, J.A. (2006) *Nat. Mater.*, **5**, 33.
- 65 Kim, D.-H., Liu, Z., Kim, Y.-S., Wu, J., Song, J., Kim, H.-S., Huang, Y., Hwang, K.-C., Zhang, Y., and Rogers, J.A. (2009) *Small*, **5**, 2841.
- 66 Kim, D.-H., Kim, Y.-S., Wu, J., Liu, Z., Song, J., Kim, H.-S., Huang, Y.Y., Hwang, K.-C., and Rogers, J.A. (2009) *Adv. Mater.*, **21**, 3703.
- 67 Ko, H.C., Shin, G., Wang, S., Stoykovich, M.P., Lee, J.W., Kim, D.-H., Ha, J.S., Huang, Y., Hwang, K.-C., and Rogers, J.A. (2009) *Small*, **5**, 2703.
- 68 Sun, J.-Y., Lu, N., Yoon, J., Oh, K.-H., Suo, Z., and Vlassak, J.J. (2009) *J. Mater. Res.*, **24**, 3338.
- 69 Uchikoga, S. (2006) in *2006 IEEE International Symposium on Power Semiconductor Devices and IC's*, IEEE, p. 1.
- 70 Park, S.-I., Xiong, Y., Kim, R.-H., Elvikis, P., Meitl, M., Kim, D.-H., Wu, J., Yoon, J., Yu, C.-J., Liu, Z., Huang, Y., Hwang, K.-C., Ferreira, P., Li, X., Choquette, K., and Rogers, J.A. (2009) *Science*, **325**, 977.
- 71 Dewire, J. and Calkins, H. (2010) *Nat. Rev. Cardiol.*, **7**, 129.
- 72 Berger, H. (1929) *Arch. Psychiatr. Nervenkr.*, **87**, 527.
- 73 Hardyck, C.D., Petrinovich, L.F., and Ellsworth, D.W. (1966) *Science*, **154**, 1467.
- 74 Searle, A., and Kirkup, L. (2000) *Physiol. Meas.*, **21**, 271.
- 75 Stroop, J.R. (1935) *J. Exp. Psychol.*, **18**, 643.
- 76 Lee, J., Wu, J., Shi, M., Yoon, J., Park, S.-I., Li, M., Liu, Z., Huang, Y., and Rogers, J.A. (2011) *Adv. Mater.*, **23**, 986.